ORIGINAL ARTICLE

Structural, Spectroscopy and Magnetic Properties of Copper Doped Nickel Ferrite by the Co-precipitation Method

J. Subhashini[1] · A. Christy Ferdinand[1] · R. Sagayaraj[2]

Abstract

The Copper doped nickel ferrites were integrated by the co-precipitation method at 900 °C in this study. XRD patterns reveal the synthesized material are in single phase, face-centered Cubic (FCC) spinel structure and got good crystallinity with 10–20 nm in size. FT-IR confirmed high (426–456 cm^{-1}), low (346–387 cm^{-1}) frequency integration of tetrahedral and octahedral voids and confirmed inverse spinel structure. The ferrimagnetic properties of all synthesized materials at different concentrations were declared by the VSM. EPR analysis confirmed that existence of paramagnetic centers proves the evidence of free radicals in the ferrite materials.

Keywords Co-precipitation · Nanoparticle · Ferrimagnetisms · VSM · Free radicals · Ferrite

1 Introduction

Ferrite and its composite ferrites are produced by various methods. Some methods, such as hydrothermal [1, 2], sol–gel [3], Auto combustion [4, 5] and co-precipitation [6, 7] are widely used by researchers. Co-precipitation is a simple and economical method of preparing various components of mixed ferrites. Therefore, the co-precipitation approach is one of the essential avenues for success produced by ferrites. Its structural properties, optical properties, thermal properties, magnetic properties and electrical properties were studied by young researchers. However, ferrite products have a legitimate interest in a wide variety of applications such as high-speed digital tapes, radio frequency circuits, optoelectronics, phase shifters, electrochemical technology, isolators, transformer cores, and superior quality filters [8]. As larger ions attempt to fill the voids left by smaller ions, the lattice constants in the resulting spinel structure increase. As the pH value was most

important in the synthesis of nanoferrite, which decreased from 11 to 9, the dielectric and magnetic losses were significantly increased to larger values [9]. The octahedral stretching vibrational mode of metal–oxygen is indicated by the band at 385–450 cm^{-1}, whereas the tetrahedral stretching vibrational mode is characterized by the band at 550–650 cm^{-1}. There were out of plane bending vibrations of O–H stretching at 1058 cm^{-1}. The H–O–H stretching mode of adsorbed or free water molecules is related with the vibrational band at 1633 cm^{-1} [10]. Metal oxide stretching vibrations (Ni–O and Fe–O) at the octahedral B-site and Fe–O stretching vibrations at the tetrahedral A-site is related to the primary and secondary absorption bands at 449 cm^{-1} and 583 cm^{-1}, respectively. Cation coordination in the ferrite form has been demonstrated [11]. Nickel ferrite is an integrated and occupied on different platforms. (Fe^{2+}) $(Ni^{2+}Fe^{3+})$ O_4, this compound is occupied by a half-half tetrahedral (A) site and an octahedral site (B) of iron (Fe^{3+}). Divalent cations $(Fe^{2+}$ occupy the tetrahedral site) while divalent and trivalent cations $(Ni^{2+}$ and $Fe^{3+})$ occupy the [12, 13] octahedral site (B site). Since the divalent and trivalent cations are displaced by each other due to the small radii of the cations, the products estimate the length in the grain parameter with subject to Vegard's law. Therefore, it shows the formation of ferromagnetism; an antiparallel spins between Fe^{3+} in the tetrahedral site and Ni^{2+} in the octahedral site [14]. The ferrite surface affects the particle size. The structural and ionic properties on the surface of the particles lead to the misperception of the grain symmetry presenting the anisotropy. A significant

✉ A. Christy Ferdinand
christyferdinand2@gmail.com

✉ R. Sagayaraj
sagayarajnancy@gmail.com

1 PG & Research Department of Physics, Periyar Arts College, Cuddalore, Tamilnadu 607001, India

2 PG & Research Department of Physics, St. Joseph's College of Arts and Science (Autonomous), Cuddalore, Tamilnadu 607001, India

number of properties start from the single domain nature of superparamagnetism particles and express Ni–Cu ferrites as a cubic spinel structure [15, 16]. Magnetic ferrites with Polyvinylpyrrolidone (PVP) composites are a promising possibility for their ideal magnetic and electrical properties. PVP gives various potential biomedical and bundling applications as responsive, modest, nontoxic, hydrophilic, and biocompatible [17]. The elements like Ni, Mg, Co, Zn, and Cu ferrite nanoparticles yielded higher catalytic activities by comparison with iron oxide Fe_3O_4 [18, 19]. The Zinc ferrite nanoparticles and found that the size of the Zinc ferrite is less than 15 nm with free radicals [20]. Zinc ferrite particles have removed the organic pollutant under UV-irradiation using oxalic acid and with free radicals significance [21]. The graphene plays an imperative role in the photocatalytic process absorption of visible light [22]. Methylene blue (MB) concentration has a significant effect on the rate of photodegradation and this was determined for $NiFe_2O_4$ ferrites, it's a potential application for the photo-Fenton ruin of organic pollutants from wastewater [23]. The $Ni_{0.6}Cu_{0.4}Fe_2O_4$ has a reduced coercivity and a higher saturation magnetization. However, the homogeneity and ultimate magnetic properties of ferrite ceramics are influenced by crystallite or particle size distribution and magnetic properties. It has good magnetic characteristics, and the procedure is relatively simple. When considering the effect of different Cu concentrations on the magnetic characteristics of Ni ferrite, Cu doped $Ni_{0.6}Cu_{0.4}Fe_2O_4$ has superior overall magnetic properties, forming a mixed spinel structure and so increasing the overall magnetic properties of particular ratio [24]. The tetrahedral void is associated with the higher frequency band (v_1) in the range 502–597 cm^{-1}, whereas the octahedral void is associated with the lower frequency band (v_2) in the range 439–490 cm^{-1} and confirms formation M–O bond [25]. The magnetic characteristics of $Ni_{0.5}Cu_{0.5}Fe_2O_4$ synthesized using NH_4OH are unique, with Ms and Mr values of 20.210 emu/g and 2.096 emu/g, respectively. This good magnetic characteristic could be attributable to the fact that NH_4OH is a weak electrolyte, which helps the nanoparticles remain stable [26]. The magnetization of citrate-produced ferrite ($Cu_{0.5}Ni_{0.5}Fe_2O_4$) nanoparticles is higher. The surface to volume ratio falls as particle size increases, resulting in an increase in saturation magnetization [27]. So the present study is focused in analysis on size, magnetic signature and free radicals in the ferrite matrix.
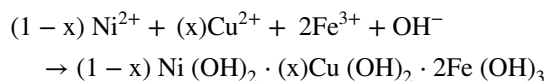
2 Experimental

2.1 Materials

Ferric sulfate monohydrate ($Fe_2(SO_4)_3 \cdot H_2O$, assay: 99%), Copper (II) sulfate pentahydrate ($CuSO_4 \cdot 5H_2O$), Nickel sulfate hexahydrate ($NiSO_4 \cdot 6H_2O$, assay: 99%) Ethanol,
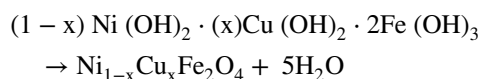
Ammonia, Polyvinylpyrrolidone ($(C_6H_9NO)_n$, assay: 98%) are purchased from sigma Aldrich respectively.

2.2 Synthesis of PVP Coated $Ni_{1-x}Cu_xFe_2O_4$ Nanoscale Particles

The PVP coated and synthesized ferrites by chemical Co-precipitation method with simple manipulations as shown Fig. 1. In this method, a beaker containing 100 ml distilled water with ferric sulfate monohydrate, nickel sulfate hexahydrate, Copper (II) sulfate pentahydrate and PVP were mixed in the ratio of 1:2. They are stirred for 1 h to gain a homogeneous solution. Now, the ammonia is slowly added drop by drop to the precursor which attains pH value 11 [28] and gets a black color solution. Then materials were washed three times by alcohol and water by using a centrifuge. And precipitates are kept in a hot air oven for 6 h and dried purpose. The magnetic materials were isolated and carried out using a bar magnet. They can make fine powder by agate mortar. Now, we have permanent materialization as a black powder of Ni–Cu ferrites. Finally, black powders have been kept in a muffle furnace annealed at 900 °C for 4 h. The Co-precipitation and ferrite equations are discussed below, Co-precipitation equations:

$$(1 - x)\, Ni^{2+} + (x)Cu^{2+} + 2Fe^{3+} + OH^- \rightarrow (1 - x)\, Ni\,(OH)_2 \cdot (x)Cu\,(OH)_2 \cdot 2Fe\,(OH)_3$$

Ferrite equations:

$$(1 - x)\, Ni\,(OH)_2 \cdot (x)Cu\,(OH)_2 \cdot 2Fe\,(OH)_3 \rightarrow Ni_{1-x}Cu_xFe_2O_4 + 5H_2O$$

3 Results and Discussion

3.1 X-ray Diffraction Analysis

Figure 2 shows the diffraction patterns of copper doped nickel ferrite annealed at 900 °C. These diffraction patterns were compared to the JCPDS: 89-4927 and identified space group Fd $\bar{3}$ m. All samples exhibits single phase with Face Centered Cubic (FCC) spinel structure [16]. The most diffraction intense peak (311) was used to find crystallite size, internal strain, lattice constant, X-ray density, unit cell volume and dislocation density. The crystallite size found by Eq. 1

$$D = K\,\lambda/\beta\,Cos\,\theta\,(nm) \tag{1}$$
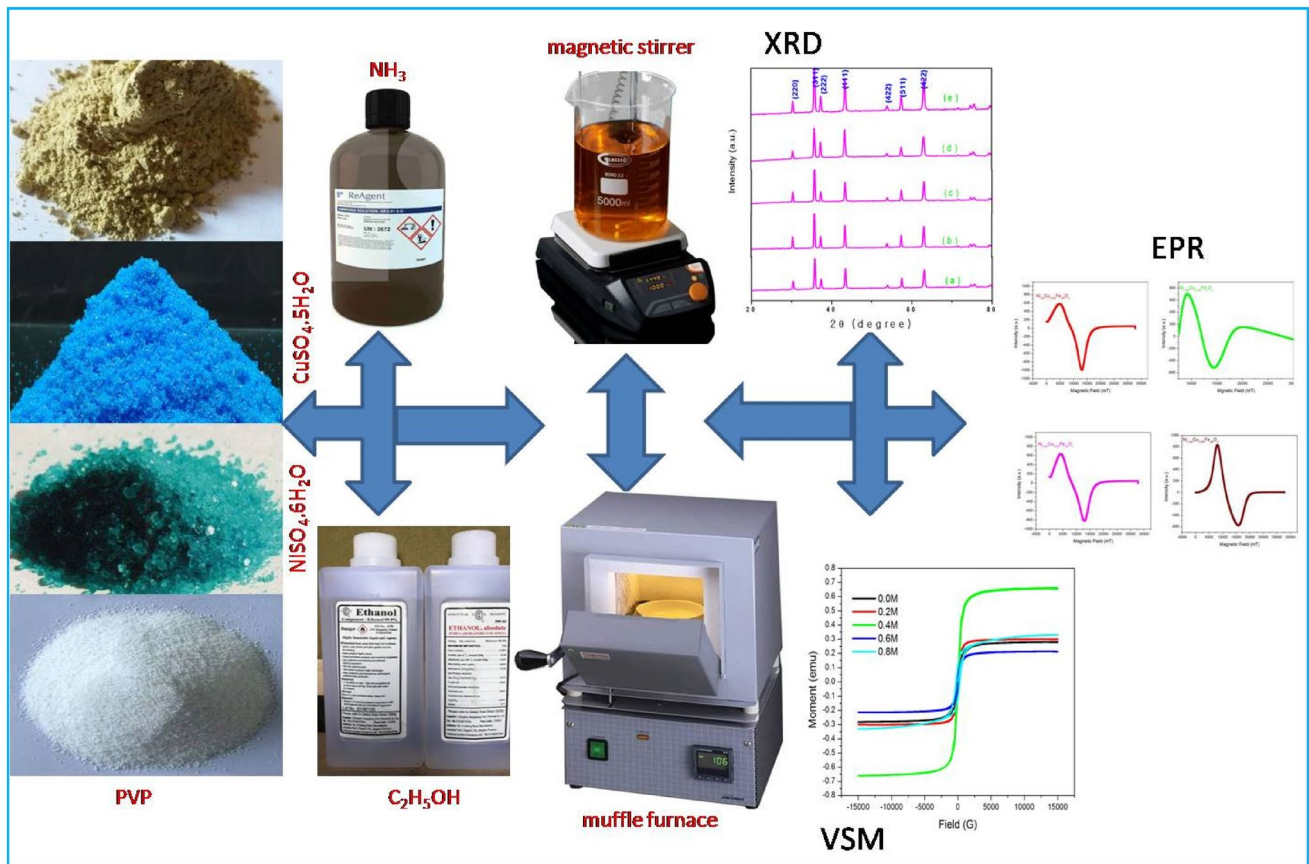
Fig. 1 Synthesis of $Ni_{1-x}Cu_xFe_2O_4$ ferrite

where λ is the X-ray wavelength, β is the width of the peak, and θ is Bragg's position of the peaks. When $x = 0$, the crystallite size is 20 nm. An increased concentration ($x > 0$) their crystallite is decreased. $x = 0.6$ has least value (10 nm) and compared other concentration ferrites. As results, copper composite is more stable than the pure sample. Diffraction angle is shift to the lower side 2θ angle. That's why crystallite size is decreased when Cu^{2+} substituted nickel ferrite [28]. By comparing the ionic radii of ($Fe^{3+} \rightarrow 60$ nm[29], $Ni^{2+} \rightarrow 70$ nm, $Cu^{2+} \rightarrow 73$ nm) metal cations in which the bigger Cu^{2+} ions are occupied "B" sites than Fe^{3+} pushed to "A" sites for example ($[A]^{tet}$ $[A, B]^{oct} O_4$). Hence, materials exhibit an inverse spinel structure [5]. These migrations of cations exhibited ferritzation for different concentrations of Cu^{2+} which are favoring the decrease crystallite size as shown in the Fig. 3 [30]. When an increase concentration up to $x = 0.6$ decrease crystallite size from 20 to 10 nm. At $x = 0.8$ tuning size is 14 nm which is correlate $x = 0.2$. The lattice constant was obtained by using Eq. 2 [6].

$$a = d \left(h^2 + K^2 + l^2\right)^{1/2} (AA) \tag{2}$$

where (h, k, l) is the Miller indices, 'a' is the lattice parameter, 'd' is inter-planar spacing. From Table 1, lattice constant is decreased from 8.536 to 8.290 Å with copper enhancement as shown in Fig. 3. By comparing the ionic radii of Ni^{2+} and Cu^{2+} ions, which is not a direct replacement of Ni by Cu. Because of the ionic size of Ni^{2+} is smaller than Cu^{2+}. The X-ray density (D_b) was estimated by [12, 30–32],

$$D_b = 8M/N a^3 \left[g/cm^3\right] \tag{3}$$

where, 8 are the quantity of atoms in a unit cell, M is the atomic weight of the composition, N is the Avogadro's number 'a' is the lattice parameter. X-ray density (D_b) shows the densification of the ferrite material. X-ray density is increased from 5.336 to 6.947 g/cm³. Materials might have assigned to be an effect of migration of ions mutually between sites and ultrafine fine crystallite size. The volume of the unit cell found by [30],

$$V = a^3 (AA)^3 \tag{4}$$

Fig. 2 X-ray Diffraction patterns of $Ni_{1-x}Cu_xFe_2O_4$ ferrite
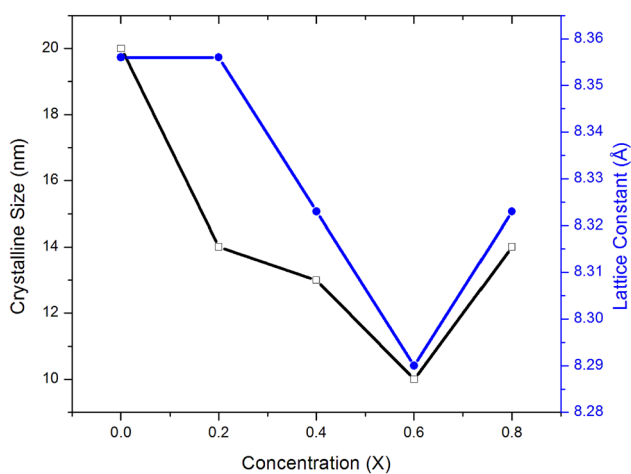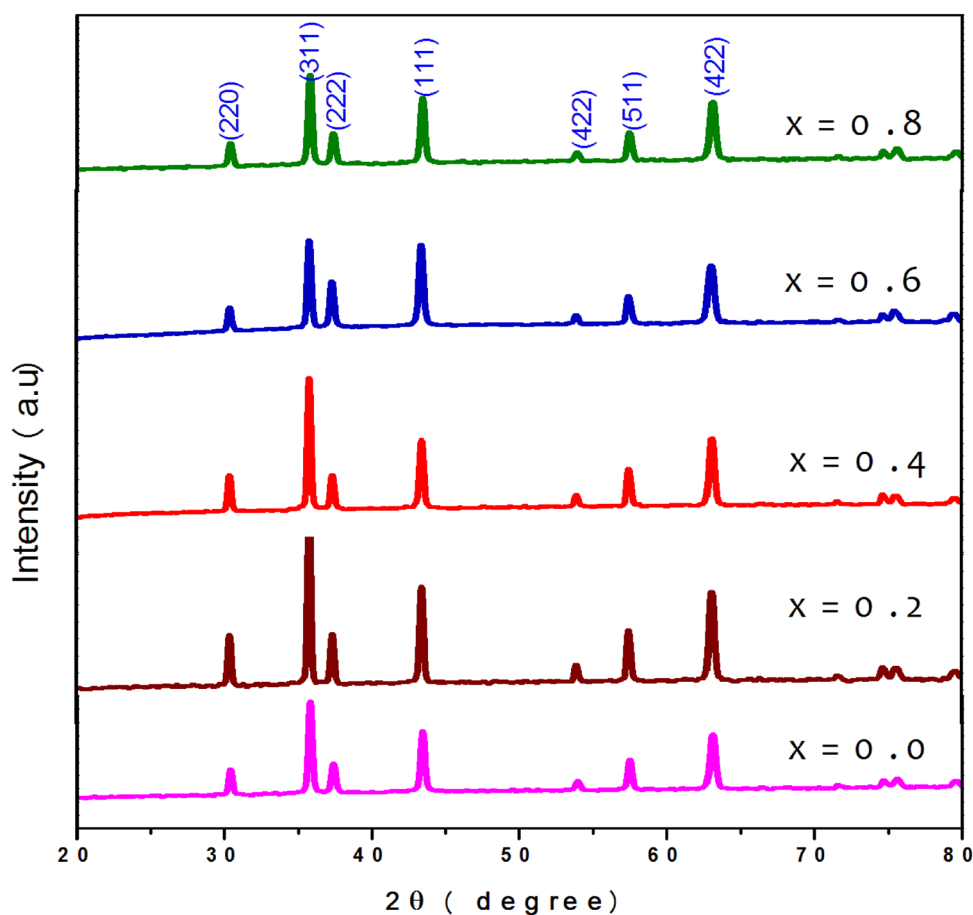
Fig. 3 Variation of crystalline size, lattice constant of $Ni_{1-x}Cu_xFe_2O_4$

From Table 1, the volume of the unit cell changes from 583.50 to 569.72 Å because of the lattice shrinking for Cu^{2+}. It causes an increase in the density of the unit cell. The lattice strain (ε) calculated by [31],

$$\varepsilon = (\beta \cos \theta)/4 \tag{5}$$

where 'β' is the width of the peak estimated in radian, and 'θ' in degrees. A lattice strain implies that the separation of the significant crystalline plane which is not indistinguishable potentially, because of the proximity (Cu^{2+}) of imperfections and stress (magnetic properties) [15]. It can view this reduction as the micro-strain of the fundamental material. The Dislocation density (δ) has been calculated by [31],

$$\delta = 15./a.t \tag{6}$$

where 'ε' is a strain, 'a' is a lattice constant, 't' is the average particle size. It shows the values of dislocation density in Table 1. These variations of dislocation density are a function of air quenching. The dislocation density uncovers which emphatically relies upon nanoscale molecule and also the rate and amount of thermal stresses developed during final quenching cycle (air), and they relief by micro plastic deformation mechanisms during that period.

Table 1 The structural parameters of $Ni_{1-x}Cu_xFe_2O_4$ ferrites

Concentration (X)	D (nm)	D_b (g/cm³)	V (Å)³	ε (No unit)	δ (nm)⁻²	a (Å)
0.0	20	5.336	583.50	0.166	0.020	8.356
0.2	14	6.784	583.50	0.214	0.026	8.356
0.4	13	6.864	576.55	0.238	0.029	8.323
0.6	10	6.947	569.72	0.309	0.038	8.290
0.8	14	6.864	576.55	0.214	0.026	8.323

Crystalline Size (D); X-ray density (D_b); Volume of the unit cell (V); Lattice Strain (ε); Dislocation density (δ); Lattice Constant (a)

Table 2 Tentative vibrational assignments of $Ni_{1-x}Cu_xFe_2O_4$ ferrites

| Concentration (X)	FTIR-Frequency band (cm⁻¹)	
	ν_1	ν_2
0.0	376	433
0.2	346	426
0.4	387	444
0.6	365	415
0.8	376	456

Vibration of tetrahedral complex (ν_1); Vibration of octahedral complex (ν_2)

3.2 FTIR Analysis

Figure 4 shows an FTIR spectrum of synthesized materials in the range of 800–350 cm⁻¹. Two metal oxide absorption bands were observed in the range 346–456 cm⁻¹ and confirmed spinel structure. Cu^{2+}–O^{2-}–Ni^{2+} represents high vibrational frequencies in tetrahedral sites, while Fe^{3+}–O^{2-}–Fe^{3+} represents low vibrational frequencies in octahedral sites [25, 33]. Higher frequency (ν_1) peaks can be seen in the range 426–456 cm⁻¹ [25], while lower frequency (ν_2) peaks can be found in the range 346–387 cm⁻¹ [12,25, 34,] Trivalent cations (Fe^{3+}) are likely to be replaced by divalent cations Cu^{2+} and Ni^{2+} at octahedral sites, permitting Fe^{3+} cations to occupy both sites. As a result materials exhibit inverse spinel ferrite structure. Jahn–Teller distortion, explain how cations are exchange at tetrahedral sites and an octahedral sites [4, 14, 35] (Table 2).

3.3 VSM Analysis

The hysteresis loops was recorded for all samples at room temperature as shown in Fig. 5. The magnetic parameters such as saturation magnetization (M_s), retentivity (M_r), coercivity (H_c), magnetic moment (μ_B), remnant ratio (R), and anisotropy constant (K) and energy product (E_p) were presented in Table 3. All the magnetic parameters were affected by Cu as substitution increases and exhibits ferrimagnetic
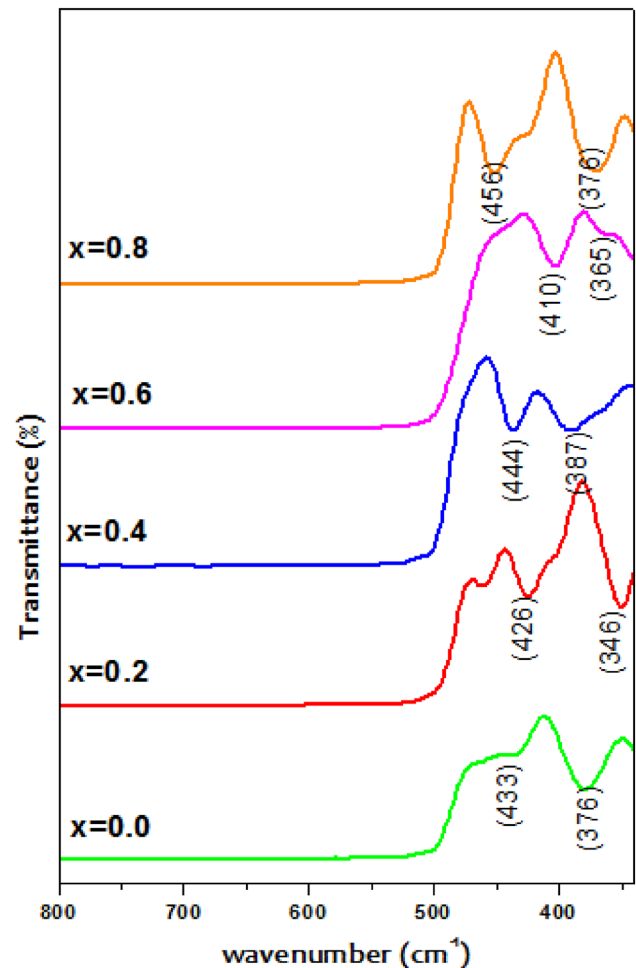

Fig. 4 FTIR Spectra of $Ni_{1-x}Cu_xFe_2O_4$ ferrite

characteristics. The ferrimagnetic properties of sample strongly depend on the cation migrations among tetrahedral and octahedral sites [36, 37]. When copper incorporated Ni-ferrite sample, the magnetization slightly increased (x = 0.0 to 0.4), the rate of magnetization increases until (x = 0.4) saturation is reached as shown as shown in Fig. 6, but other concentration sample (x = 0.6 & 0.8) the magnetization slightly decreased, materials observed a narrow hysteresis
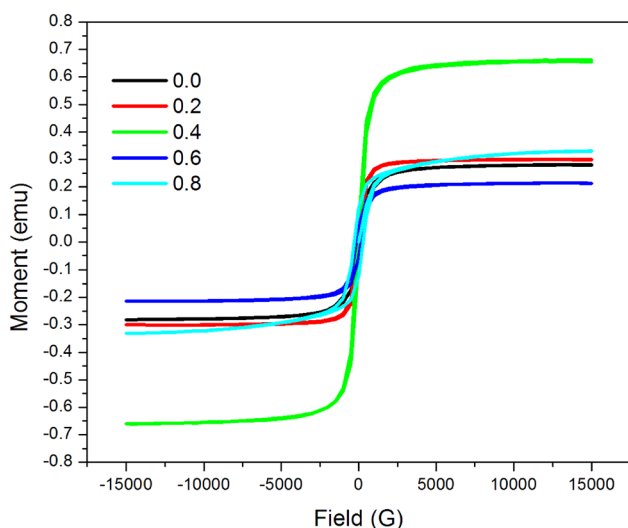
Fig. 5 VSM images of $Ni_{1-x}Cu_xFe_2O_4$ ferrite at room temperature
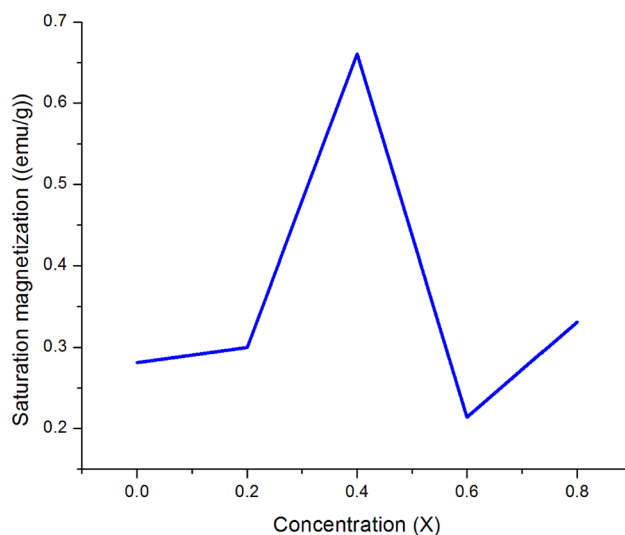
Fig. 6 Variation of saturation magnetization of $Ni_{1-x}Cu_xFe_2O_4$

loop [6]. The highest H_c values (286.29G) got from the sample ($Ni_{0.2}Cu_{0.8}Fe_2O_4$) at room temperature, but the $Ni_{0.6}Cu_{0.4}Fe_2O_4$ sample ($x = 0.4$) yielded the smallest coercivity value (71.54G) and the highest magnetic moment at room temperature as shown in Fig. 7. The coercivity value of the $Ni_{0.6}Cu_{0.4}Fe_2O_4$ ferrite was smaller than the H_c values of the $Ni_1Fe_2O_4$ ferrite, but materials were larger than the Hc values of the $NiFe_2O_4$ ferrite. Several studies have found varying coercivity values when particle size is compared. According to Ibrahim et al. $MgFe_2O_4$ had a coercivity of 104.4Oe for 29 nm particle size [46]. Pradeep et al. revealed coercivity as 202.55G for 35 nm grain size [47]. Rabanal et al. calculated a coercivity of 576.7Oe for particles with an average size of 80 nm [48]. As the above values show, coercivity is proportional to grain or particle size. The values of the remnant ratio ranges from 0.249 to 0.375 as listed in Table 3. The remnant ratio is minimum at x = 0.4 due to small imbalance of cations with multi-domain cases [29, 38] in the ferrite system as shown in Fig. 8. For instance, retentivity (M_r) of the 20 nm Ni ferrite made by co-precipitation gives a value of about 70.325E-3 emu/g at room
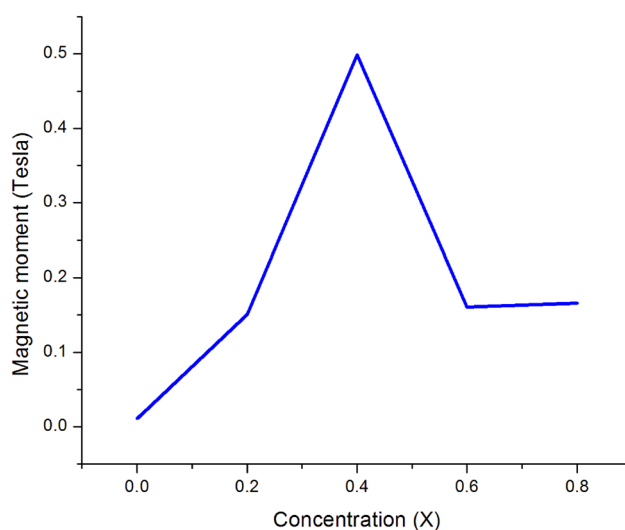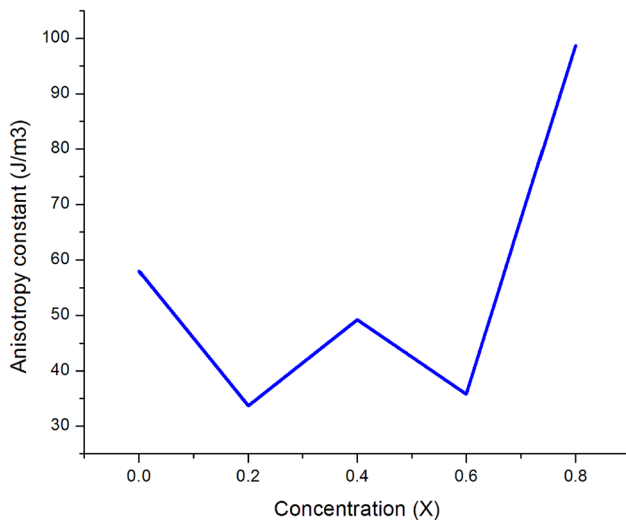

Fig. 7 Variation of magnetic moment of $Ni_{1-x}Cu_xFe_2O_4$

Table 3 VSM analysis of $Ni_{1-x}Cu_xFe_2O_4$ ferrites

Concentration (X)	M_s (emu/g)	M_r (emu/g)	H_c (G)	μB Tesla	R No unit	K J/m³	E_P (MGOe)
0.0	0.281	70.325E-3	197.72	0.011	0.249	58.00	13.904
0.2	0.300	57.522E-3	107.57	0.151	0.191	33.69	6.187
0.4	0.661	66.539E-3	071.54	0.499	0.100	49.29	4.760
0.6	0.214	57.951E-3	160.09	0.161	0.270	35.73	9.277
0.8	0.331	0.12422	286.29	0.166	0.375	98.71	35.562

Saturation magnetization (M_s), Retentivity (M_r), Coercivity (H_c), Magnetic moment (μ_B), Remnant ratio (R), Anisotropy constant (K) and Energy product (E_p)
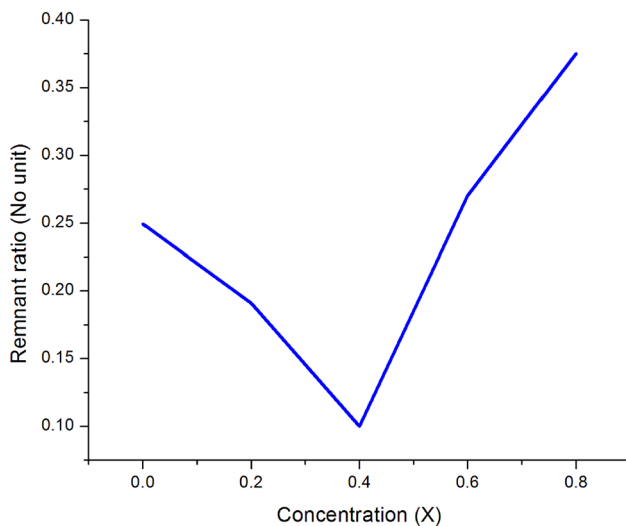
Fig. 8 Variation of remnant ratio of $Ni_{1-x}Cu_xFe_2O_4$

Fig. 9 Variation of Anisotropy constant of $Ni_{1-x}Cu_xFe_2O_4$

temperature, because, 13 nm $Ni_{0.6}Cu_{0.4}Fe_2O_4$ ferrite made by the reverse micelles gives 66.539E-3 emu/g of retentivity for similar conditions and hence the magnetic moment (μ_B) is also enhanced [39]. A nonlinear variation in the anisotropy constant (K) can explain the base on the reduction particle size, magnetic behavior, demagnetizing field and surface effects may induce a spin disorder in the surface layer resulting in reduced anisotropy and occurs up to $x = 0.6$ as shown in the Fig. 9. When an anti-ferromagnetic signature and ferromagnetic signature interacts (ferrimagnetic), it results in the maximum energy product which is obtained for

the maximum amount of magnetic energy stored in a material. So, its value revealed for potential significance of the Energy product (E_P) which is an increased from 13.904 to 35.562 MGOe [40].
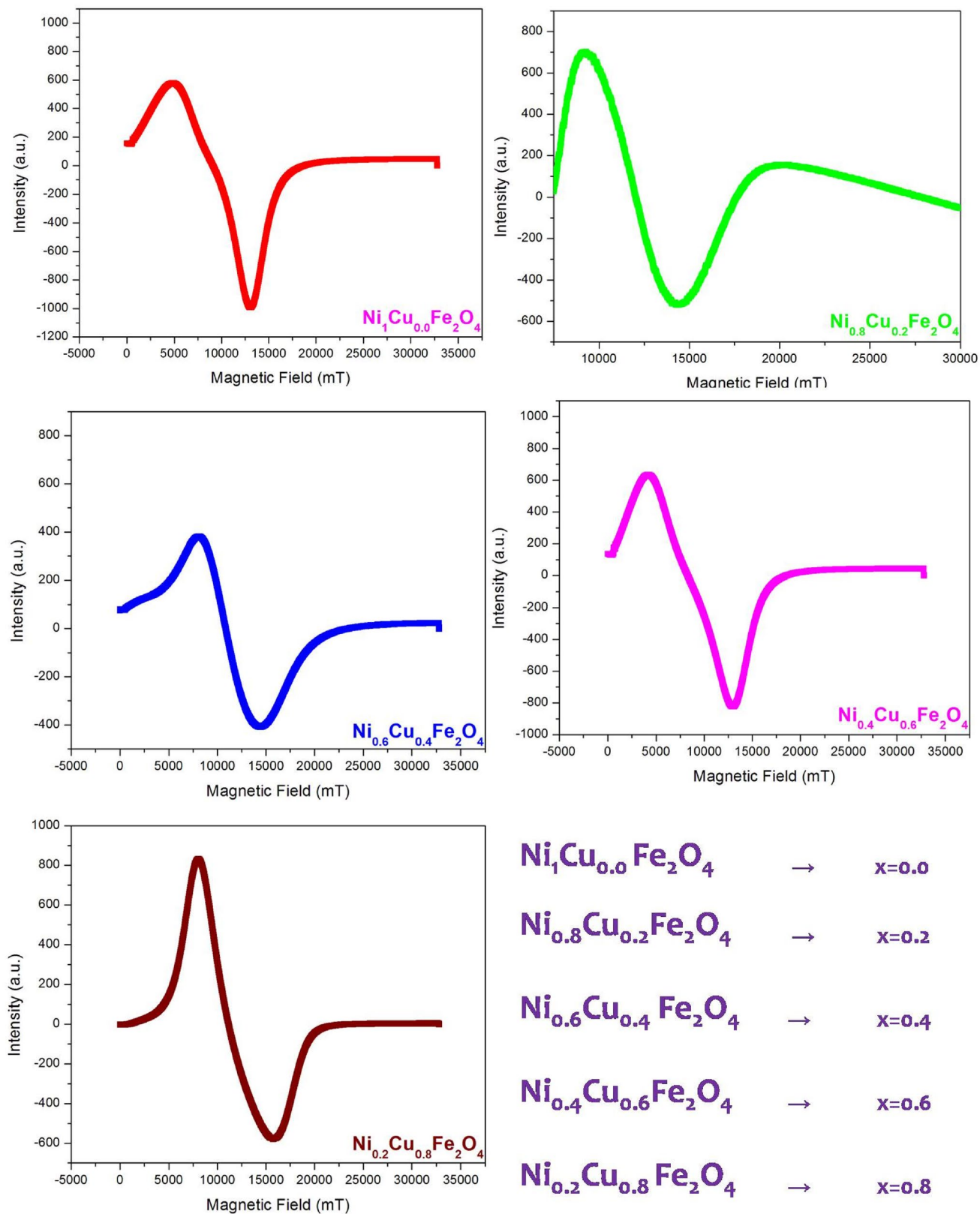
3.4 EPR Analysis

Figure 10 shows the first derivative EPR spectra of $Ni_{1-x}Cu_xFe_2O_4$ are recorded at room temperature. Materials restrict to a survey of ions or molecules having more unpaired electrons. It is used to explore the character of direction in the paramagnetic system. The g factor was computed using the accompanying condition [23, 41],

$$g = h\nu/H\beta \qquad (7)$$

where h is Planck's constant, ν is the frequency; H is the resonance magnetic field and β is the Bohr magnetron. Then, g factor gives information by viewing the sub-atomic movement, the paramagnetic properties and the symmetry/asymmetry of ions. From the EPR spectra, the materials show a sharp symmetrical line and a wide asymmetrical line with a slight move from the free electron position ($g = 2.0023$). The symmetric line changing into asymmetric lines, on the justification that radicals created in the materials for Cu^{2+} incorporated $NiFe_2O_4$ [42]. The super-paramagnetic behavior of the materials is affirmed through the g-values (lesser than 2) found out from the EPR spectra [43]. From Table 4, It has recorded g-factor values and compared with different molar ratio and conclude that the dipolar interaction between Fe^{3+} ions (like spins) dominates for the materials ($x = 0.0$, 0.4) while dipolar interaction between ($Fe^{2+} \leftrightarrow Ni^{2+}$; $Ni^{2+} \leftrightarrow Cu^{2+}$, $Cu^{2+} \leftrightarrow Fe^{2+}$) cations (unlike spin) dominates for sample ($x = 0.2$; 0.6; 0.8) [44]. From Fig. 11 observed g values are linearly maintained as much as the oxygen mindfulness over the samples which was expanded upon the stoichiometric concentration [45].

4 Conclusion

The copper doped nickel ferrites were successfully employed by the Co-precipitation method. These materials have distinct structural and magnetic properties that can be easily controlled by varying the concentration of the precursor. The XRD diffraction pattern revealed crystallites with sizes ranging from 10 to 20 nm and higher crystallinity. The stretching vibration bands were detected in FTIR at 426–456 cm^{-1} for Cu^{2+}–O^{2-}–Ni^{2+} and 346–387 cm^{-1} for Fe^{3+}–O^{2-}–Fe^{3+} at tetrahedral and octahedral frequencies, respectively. VSM
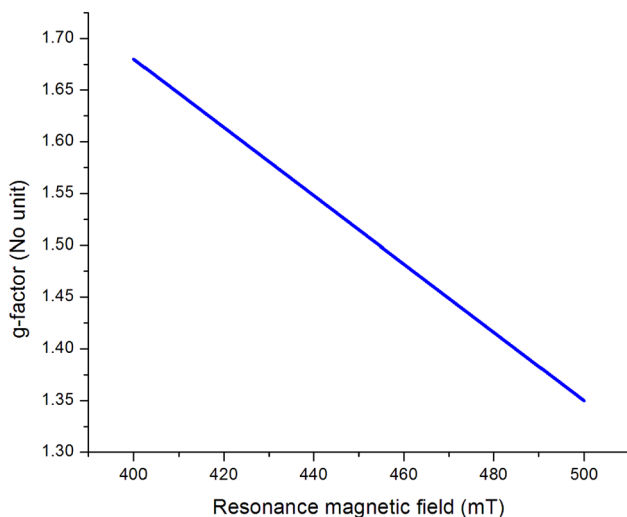
Fig. 10 EPR images of $Ni_{1-x}Cu_xFe_2O_4$ ferrite at room temperature

Table 4 g-factor analysis of $Ni_{1-x}Cu_xFe_2O_4$ ferrites

Concentration (X)	g-factor analysis		
	Frequency (MHz)	Resonance magnetic field mT	g-factor No unit
0.0	9454.18	500	1.35
0.2	9453.37	400	1.68
0.4	9454.14	500	1.35
0.6	9452.77	400	1.68
0.8	9450.94	400	1.68

Fig. 11 Variation of g-factor of $Ni_{1-x}Cu_xFe_2O_4$

analysis investigated soft magnetic signatures with ferrimagnetic properties and yielded various magnetic parameters. EPR analysis revealed the paramagnetic centre and free radical production in the ferrite system.

Declarations

Conflict of Interest The authors declare that they have no known competing financial interests or personal relationships that could have appeared to influence the work reported in this paper.

Ethical Approval This article does not contain any studies with human volunteers or animals being involved by any of the authors.

Informed Consent None.

References

1. Nejati K, Zabihi R (2012) Preparation and magnetic properties of nano size nickel ferrite particles using hydrothermal method. Chem Cent J 6:23–23
2. Pervaiz E, Gul IH, Anwar H (2013) Hydrothermal synthesis and characterization of $CoFe_2O_4$ nanoparticles and nanorods. J Supercond Novel Magn 26:415–424
3. Rao P, Godbole RV, Bhagwat S (2016) Copper doped nickel ferrite nano-crystalline thin films: a potential gas sensor towards reducing gases. Mater Chem Phys 171:260–266
4. Hashim M, Raghasudha M, Shah J, Shirsath SE, Ravinder D, Kumar S, Meena SS, Bhatt P, Alimuddin, Kumar R, Kotnala RK (2018) High temperature dielectric studies of indium-substituted NiCuZn nanoferrites. J Phys Chem Solids 112:29–36
5. Sivakumar V, Ramesh R, Ramanand A, Ponnusamy S, Muthamizhchelvan C (2011) Preparation and properties of nickel ferrite ($NiFe_2O_4$) nanoparticles via sol–gel auto-combustion method. Mater Res Bull 46:2204–2207
6. Lassoued A, Lassoued MS, Karolak F, García-Granda S, Dkhil B, Ammar S, Gadri S (2017) Synthesis, structural, optical, morphological and magnetic characterization of copper substituted nickel ferrite ($Cu_xNi_{1-x}Fe_2O_4$) through Co-precipitation method. J Mater Sci: Mater Electron 28:18480–18488
7. Sagayaraj R, Dhineshkumar T, Prakash A, Aravazhi S, Chandrasekaran G, Jayarajan D, Sebastian S (2020) Fabrication, microstructure, morphological and magnetic properties of W-type ferrite by co-precipitation method: antibacterial activity. Chem Phys Lett 759:137944
8. Hcini S, Omri A, Boudard M, Bouazizi ML, Dhahri A, Touileb K (2018) Microstructural, magnetic and electrical properties of $Zn_{0.4}M_{0.3}Co_{0.3}Fe_2O_4$ (M = Ni and Cu) ferrites synthesized by sol–gel method. J Mater Sci: Mater Electron 29:6879–6891
9. Chandra Babu Naidu K, Madhuri W (2017) Microwave processed bulk and nano Ni Mg ferrites: a comparative study on X-band electromagnetic interference shielding properties. Mater Chem Phys 187:164–176. https://doi.org/10.1016/j.matchemphys.2016.11.062
10. Rajivgandhi GN, Ramachandran G, Kanisha CC, Alharbi NS, Kadaikunnan S, Khaled JM, Li W-J (2021) Effect of Ti and Cu doping on the structural, optical, morphological and anti-bacterial properties of nickel ferrite nanoparticles. Results Phys 23:104065. https://doi.org/10.1016/j.rinp.2021.104065
11. Babu Naidu KC, Madhuri W (2017) Hydrothermal synthesis of NiFe2O4nano-particles: structural, morphological, optical, electrical and magnetic properties. Bull Mater Sci 40(2):417–425. https://doi.org/10.1007/s12034-017-1374-4
12. Kumar GR, Kumar KV, Venudhar YC (2012) Synthesis, structural and magnetic properties of copper substituted nickel ferrites by sol-gel method. Mater Sci Appl 03:87–91
13. Zakiyah LB, Saion E, Al-Hada NM, Gharibshahi E, Salem A, Soltani N, Gene S (2015) Up-scalable synthesis of size-controlled copper ferrite nanocrystals by thermal treatment method. Mater Sci Semicond Process 40:564–569
14. Anjum S, Rashid A, Bashir F, Riaz S, Pervaiz M, Zia R (2014) Effect of Cu-doped nickel ferrites on structural, magnetic, and dielectric properties. IEEE Trans Magn 50:1–4
15. Wang H, Zhu D, Zhou W, Luo F (2015) Synthesis and microwave absorbing properties of Ni–Cu ferrite/MWCNTs composites. J Mater Sci: Mater Electron 26:7698–7704
16. Ahamad HS, Meshram NS, Bankar SB, Dhoble SJ, Rewatkar KG (2017) Structural properties of $Cu_xNi_{1-x}Fe_2O_4$ nano ferrites prepared by urea-gel microwave auto combustion method. Ferroelectrics 516:67–73

17. Madhu BJ, Ashwini ST, Shruthi B, Divyashree BS, Manjunath A, Jayanna HS (2014) Structural, dielectric and electromagnetic shielding properties of Ni–Cu nanoferrite /PVP composites. Mater Sci Eng, B 186:1–6

18. Xu S, Shangguan W, Yuan J, Chen M, Shi J (2007) Preparation and photocatalytic properties of magnetically separable TiO_2 supported on nickel ferrite. Chin J Chem Eng 15:190–195

19. Cheng R, Fan X, Wang M, Li M, Tian J, Zhang L (2016) Facile construction of $CuFe_2O_4/g$-C_3N_4 photocatalyst for enhanced visible-light hydrogen evolution. RSC Adv 6:18990–18995

20. Veinger AI, Zabrodskii AG, Tisnek TV, Mokhov EN (2004) Specific features of electron spin resonance in 4H-SiC in the vicinity of the insulator-metal phase transition: II. Analysis of the width and shape of lines. Semiconductors 38:782–787

21. Liu SQ, Xiao B, Feng LR, Zhou SS, Chen ZG, Liu CG, Chen F, Wu ZY, Xu N, Oh WO, Meng ZD (2013) Graphene oxide enhances the Fenton-like photocatalytic activity of nickel ferrite for degradation of dyes under visible light irradiation. Carbon 64:197–206

22. Xiao B, Liu SQ (2014) Enhancing the photocatalytic activity of nickel ferrite doped with graphene. Asian J Chem 26:1391–1393

23. Sharma R, Bansal S, Singhal S (2015) Tailoring the photo-Fenton activity of spinel ferrites (MFe_2O_4) by incorporating different cations (M = Cu, Zn, Ni and Co) in the structure. RSC Adv 5:6006–6018

24. Li Z, Zhao K, Chen P, Guo J (2012) Performance of NiCu ferrite fine particles and ceramics synthesized using egg white. Procedia Eng 27:1492–1501. https://doi.org/10.1016/j.proeng.2011.12.613

25. Gaikwad PV, Kamble RJ, Gavade SJM, Sabale SR, Kamble PD (2018) Magneto-structural properties and photocatalytic performance of sol-gel synthesized cobalt substituted Ni Cu ferrites for degradation of methylene blue under sunlight. Physica B. https://doi.org/10.1016/j.physb.2018.11.032

26. Wahaab FA, Adebayo LL, Adekoya AA, Hakeem IG, Alqasem B, Obalalu AM (2020) Physiochemical properties and electromagnetic wave absorption performance of Ni0.5Cu0.5Fe2O4 nanoparticles at X-band frequency. J Alloys Compounds 836:155272. https://doi.org/10.1016/j.jallcom.2020.155272

27. Manju BG, Raji P (2018) Synthesis and magnetic properties of nano-sized Cu 0.5 Ni 0.5 Fe 2 O 4 via citrate and aloe vera: a comparative study. Ceramics Int 44(7):7329–7333. https://doi.org/10.1016/j.ceramint.2018.01.201

28. Sagayaraj R, Aravazhi S, Chandrasekaran G (2021) Microstructure and magnetic properties of $Cu_{0.5}Co_{0.3}Mo_{0.2}Fe_2O_4$ ferrite nanoparticles synthesized by Coprecipitation method. Appl Phys A 127:1–8

29. Sagayaraj R, Aravazhi S, Chandrasekaran G (2021) Review on structural and magnetic properties of (Co–Zn) ferrite nanoparticles. Int Nano Lett 11(4):307–319

30. Sridhar R, Ravinder D, Kumar KV (2012) Synthesis and characterization of copper substituted nickel nano-ferrites by citrate-gel technique. Adv Mater Phys Chem 02:192–199

31. Batoo KM, El-sadek M-SA (2013) Electrical and magnetic transport properties of Ni–Cu–Mg ferrite nanoparticles prepared by sol–gel method. J Alloy Compd 566:112–119

32. Hankare PP, Sanadi KR, Pandav RS, Patil NM, Garadkar KM, Mulla IS (2012) Structural, electrical and magnetic properties of cadmium substituted copper ferrite by sol–gel method. J Alloy Compd 540:290–296

33. Velhal NB, Patil ND, Shelke AR, Deshpande NG, Puri VR (2015) Structural, dielectric and magnetic properties of nickel substituted cobalt ferrite nanoparticles: effect of nickel concentration. AIP Adv 5:097166

34. Devmunde BH, Raut AV, Birajdar SD, Shukla SJ, Shengule DR, Jadhav KM (2016) Structural, electrical, dielectric, and magnetic properties of Cd^{2+} substituted nickel ferrite nanoparticles. J Nanoparticles 2016:1–8

35. Almeida TP, Fay MW, Zhu Y, Brown PD (2012) Hydrothermal synthesis of mixed cobalt-nickel ferrite nanoparticles. J Phys: Conf Ser 371:012074

36. Udhayan S, Udhayan S, Udayakumar R, Sagayaraj R, Gurusamy K et al (2021) Evaluation of bioactive potential of a Tragia involucrata healthy leaf extract @ ZnO nanoparticles. BioNanoSci 11:703–719. https://doi.org/10.1007/s12668-021-00864-z

37. Sagayaraj R, Aravazhi S, Praveen P, Chandrasekaran G (2018) Structural, morphological and magnetic characters of PVP coated $ZnFe_2O_4$ nanoparticles. J Mater Sci: Mater Electron 29:2151–2158

38. Murugesan C, MDgazzali PM, Chandrasekaran G (2013) Influence of oxidizer to fuel ratio on structural and magnetic properties of Mn–Zn ferrite nanoparticles. J Mater Sci: Mater Electron 24:3136–3141

39. Goodarz Naseri M, Saion EB, Ahangar HA, Hashim M, Shaari AH (2011) Synthesis and characterization of manganese ferrite nanoparticles by thermal treatment method. J Magn Magn Mater 323:1745–1749

40. Elsaid Bakeer D, Abou-Aly AI, Mohammed NH, Awad R, Hasebbo M (2017) Characterization and magnetic properties of nanoferrite $ZnFe_{2-x}La_xO_4$ prepared by co-precipitation method. J Supercond Novel Magn 30:893–902

41. Sagayaraj R, Jegadheeswari M, Aravazhi S, Chandrasekaran G, Dhanalakshmi A (2020) Structural, spectroscopic and magnetic study of nanocrystalline terbium-nickel ferrite by oxalate co-precipitation method. Chem Afr 3:955–963

42. Elilarassi R, Chandrasekaran G (2017) Influence of nickel doping on the structural, optical and magnetic properties of TiO_2 diluted magnetic semiconductor nanoparticles prepared by high energy ball-milling technique. J Mater Sci: Mater Electron 28:14536–14542

43. Sanpo N, Berndt CC, Wang J (2012) Microstructural and antibacterial properties of zinc-substituted cobalt ferrite nanopowders synthesized by sol-gel methods. J Appl Phys 112:084333

44. Sagayaraj R, Aravazhi S, Selva Kumar C, Senthil Kumar S, Chandrasekaran G (2019) Tuning of ferrites ($Co_xFe_{3-x}O_4$) nanoparticles by co precipitation technique. SN Appl Sci 1:271

45. Sagayaraj R, Aravazhi S, Chandrasekaran G (2019) Effect of zinc content on structural, functional, morphological, resonance, thermal and magnetic properties of $Co_{1-x}Zn_xFe_2O_4$/PVP nanocomposites. J Inorg Organomet Polym Mater 29:2252–2261

46. Waheed IF et al (2019) Synthesis of Mg-Ferrite nanoparticles via auto combustion method and investigation their structural, morphological and magnetic properties. Tikrit J Pure Sci 24:52–58

47. Pradeep A, Priyadharsini P, Chandrasekaran G (2008) Sol-gel route of synthesis of nanoparticles of $MgFe_2O_4$ and XRD, FTIR and VSM study. J Magn Magn Mater 320:2774–2779

48. Rabanal ME, Várez A, Levenfeld B, Torralba JM (2003) Magnetic properties of Mg ferrite after milling process. J Mater Process Technol 143–144:470–474